Original Paper

Multifractal Analysis of Pore Structure in Middle- and High-Rank Coal by Mercury Intrusion Porosimetry and Low-Pressure N$_2$ Adsorption

Shasha Zhang [ID],[1,2,3] **Huan Liu,**[4] **Zhehui Jin,**[3] **and Caifang Wu**[1,2,5]

It is of great significance to study the pore heterogeneity of coal because it affects coalbed methane exploration and exploitation. In this study, mercury intrusion porosimetry (MIP) and low-pressure N$_2$ adsorption methods were adopted to analyze the multifractal characteristics of coal pore structures with different coalification degrees. Next, a comparison was made between the two methods regarding pore structure heterogeneity. The relationships among multifractal parameters and coal ranks, proximate analysis, coal compositions, and pore structures were discussed further. The results show that the multifractal parameters of pore structures determined using the two methods had no obvious correlations. However, they were all found to be influenced by coalification degree. As coalification degree increased, the heterogeneity and complexity of the pore structures increased. Micropores measured by the MIP method had dominantly negative effects on pore connectivity and homogeneity. Meanwhile, the influencing effects of transitional pores, mesopores, and macropores were observed to be the opposite. In addition, increases in vitrinite content could potentially decrease pore connectivity and increase pore complexity, while increases in inertinite content have the opposite effects.

KEY WORDS: Pore structure, Multifractal characterization, Coalification degree, Mercury intrusion porosimetry, Low-pressure N$_2$ adsorption.

INTRODUCTION

Coalbed methane (CBM) has attracted a great deal of attention due to significant demands for cleaner energy. Its favorable properties of abundant resources worldwide, wide usage, environmentally friendly components, and so on, have increased the global interest in CBM (Gao et al., 2020; Rezaei et al., 2020). It is acknowledged widely that, among the three existential states in coal beds (free state, absorbed state, and dissolved state), absorbed gas in coal matrix plays a dominant role (Davis & Gerlach, 2018; Moore, 2012). Pores in coal matrix blocks have a broad range of size distributions, which can be classified as (Hodot, 1961): macropores

[1]Key Laboratory of Coalbed Methane Resources and Reservoir Formation Process, Ministry of Education, China University of Mining and Technology, Xuzhou 221008, Jiangsu, People's Republic of China.
[2]School of Resources and Earth Science, China University of Mining and Technology, Xuzhou 221116, Jiangsu, People's Republic of China.
[3]School of Mining and Petroleum Engineering, University of Alberta, Edmonton, AB, Canada.
[4]First Geological Environment Survey Institute of Henan Bureau of Geo-Exploration and Mineral Development, Zhengzhou 450003, Henan, People's Republic of China.
[5]To whom correspondence should be addressed; e-mail: caifangwu@sina.com

(> 1000 nm); mesopores (100–1000 nm); transnational pores (10–100 nm); and micropores (< 10 nm). The highly heterogeneous characteristics of pores have important effects on gas adsorption, storage, and transportation (Wang et al., 2014). To that end, understanding pore structures and distributions in coal is critical to understanding gas holding capacities, gas desorption, gas flow, and recovery (Clarkson & Bustin, 1999; Moore, 2012; Pang et al., 2021).

However, it is inappropriate to characterize pore structures simply using a single method due to the wide pore size range. During the past decade, pore characterization methods such as imaging, fluid intrusive, and non-fluid intrusive methods have been applied widely in the field of CBM exploration (San José Blach et al., 2020; Chen et al., 2019; Li et al., 2021; Martínez et al., 2010; Oluwadebi et al., 2019; Vishal et al., 2019; Vranjes-Wessely et al., 2020; Zhang et al., 2020a, 2020b; Zhao et al., 2018, 2021a, 2021b). Among these methods, mercury intrusion porosimetry (MIP) can measure pores with diameters from 3 nm to several hundred microns. In addition, low-pressure nitrogen adsorption (LPN$_2$A) showed better performance for pores with diameters less than 350 nm. Therefore, a combination of these two methods can potentially provide highly accurate results for pore structures.

Meanwhile, the fractal theory provides more details to fully understand the complexity of pore structure. Previous researchers conducted various researches on pore structures based on statistical methods. However, it is inaccurate to reflect pore structural information from different regions due to the limitations of those methods. To address those issues, multifractal analysis has been used widely to study accurately and comprehensively the complexity and heterogeneity of pore structures (Duan et al., 2021; Li et al., 2021; Liu et al., 2018a, 2018b; Yu et al., 2018; Zhang et al., 2021; Zhao et al., 2021a, 2021b). Zhao et al. (2019) conducted multifractal analysis on low-temperature N$_2$ adsorption and NMR T$_2$ distributions of pore structure distributions in Middle Bakken shales. Based on the MIP test method, Zhang et al. (2021) used multifractal theory to analyze the multifractal characteristics of pore structure with different coal ranks and believed that coal pore structures are majorly affected by coalification degrees. Based on gas adsorption methods, Li et al. (2021) studied the heterogeneity of micro- and mesopore structures of tectonically deformed coals and suggested that multifractal properties of pore

volume (PV) and specific surface area (SSA) distributions are influenced significantly by pore structural changes related to coal deformation. The above-mentioned researchers confirmed the effectiveness of multifractal analysis to characterize the heterogeneity of porous media. However, only a few studies have focused on pore structure heterogeneity with different coal ranks, especially with different test methods. Therefore, further research regarding the multifractal characteristics of pore structures with different coal ranks is required.

At present, the Western Guizhou–Eastern Yunnan is one of the most promising CBM development regions in China (Cheng et al., 2020; Ju et al., 2018; Zhang et al., 2020a, 2020b). Understanding the pore structure characteristics of different coal ranks is important for the exploration and development of CBM in that region. In this study, 16 samples of middle- and high-rank coal samples were collected and analyzed by multifractal theory using MIP and LPN$_2$A methods. The main goals of this paper were: (1) to analyze the pore size distribution (PSD) characteristics of middle- and high-rank coal samples from the Enhong and Laochang mining areas based on a combination of LPN$_2$A and MIP data; (2) to obtain the multifractal characteristics; and (3) to discuss the relationships between the multifractal parameters and physical properties of the samples.

MATERIALS, EXPERIMENTAL METHODS, AND ANALYSES

Sample Collection and Preparation

To investigate the multifractal characteristics of middle- and high-rank coal samples, 16 coal samples were collected from Eastern Yunnan and Western Guizhou. The middle-rank coal samples were freshly collected from the Axing (AX), Zhenxing (ZX), Tuanjie (TJ), Qiangyuan (QY), Jiaxing (JX), Alingde (ALD), Bumuga (BMG), and Qingpingyi (QPY) coal mines in the Enhong mining area. The high-rank coal samples were obtained from the Dage (DG), Danshuo (DS), Hongfa (HF), Pubai (PB), Sebu (SB), Shewu (SW), Xiongdong (XDO), and Xiongda (XDA) coal mines in the Laochang mining area of Eastern Yunnan, China (Fig. 1). It is worth noting that samples BMG and PB were more likely to be deformed. The collected samples were
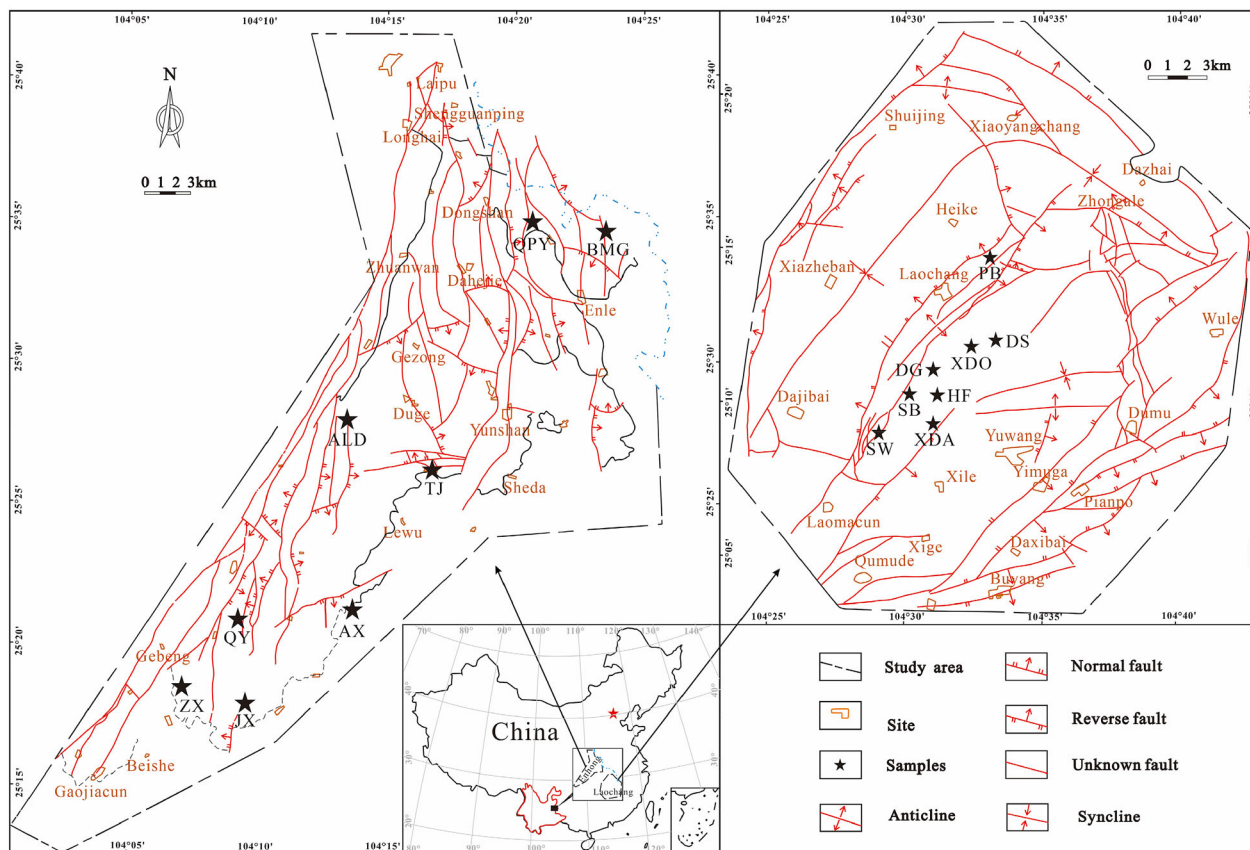
Figure 1. Tectonic outline of the study area and distribution of the samples.

sealed immediately and dispatched to laboratory for the next step(s).

Experimental Methods and Analyses

The maximum vitrinite reflectance ($R_{o,max}$) and coal macerals, proximate analysis of moisture content (M_{ad}), dry base ash (A_d), dry ash-free basis volatile (V_{daf}) and fixed carbon content (FC_d) were determined according to the standards ISO 7404–5:2009, ISO 7404–3:2009, ISO 11722:2013, ISO 1171:2010, and ISO 562:2010.

The 16 samples for MIP test were first crushed (2 mm) and weighed (1–2 g), then dried at 70 °C in a vacuum for 12 h. The MIP measurement was taken with an Autopore 9500 mercury intrusion tester following the standard ISO 15901–1:2016. The lowest limit of the pore diameters measured by the MIP test was 3 nm and the upper limit was up to several hundred microns.

The LPN$_2$A measurements were conducted on an Autosorb-IQ specific surface area and porosimeter analyzer under different relative pressures (P/P_0, where P is actual gas pressure and P_0 is vapor pressure of the adsorbing gas) ranging from 0 to 0.99 at 77°K according to ISO 15901–2:2006. Prior to the experiment, all the samples were sized to 60–80 mesh and dried in an oven at 105 for 12 h to remove moisture. Then, the samples were evacuated in a container under high vacuum at 105 for 12 h. The measurable pore sizes of N$_2$ adsorption ranged from 3 to 350 nm. In addition, the PV and SSA were obtained based on different adsorption theories. In this paper, the Barrett–Joyner–Halenda (BJH) model was used to calculate the PSD, PV, and pore SSA. The Brunauer–Emmett–Teller (BET) theory was used to obtain adsorption average pore aperture.

Multifractal analysis provides more distribution information of a target system than fractal models (Posadas et al., 2001). The details and application

method of multifractal theory can be found in previous researches (e.g., Muller, 1996).

RESULTS AND ANALYSIS

Basic Properties

The $R_{o,max}$ of the middle- and high-rank coal samples varied in the ranges of 0.99–1.27% and 2.19–2.59%, respectively (Table 1). For all 16 samples, vitrinite was the most dominant maceral composition, with 45.9–68.6% for middle-rank coal samples and 72.5–87.2% for high-rank samples. Inertinite varied within the ranges of 21.5–30.0% and 6.6–23.1% for middle- and high-rank coal samples, respectively. Some of the middle-rank coal samples contained 2.7–9.9% (average 4.65%) exinite. The minerals contained in all of samples varied in the range of 0.6–18.7%, with average of 7.4%. The proximate analysis results showed that M_{ad}, A_d, V_{daf} and FC_d of all the samples were in the ranges of 0.63–1.54% (average 0.99%), 6.34–32.82 (average 14.3%), 6.88–30.23 (average 16.9%), and 50.34–84.06 (average 71.2%), respectively. There was a strong positive relationship between A_d and mineral content with $R^2 = 0.73$ (Fig. 2a). With increasing coalification degrees, V_{daf} decreased significantly ($R^2 = 0.96$) (Fig. 2b), while M_{ad} first decreased slightly and then increased (Fig. 2c).

Characteristics of Pore Structures in Middle- and High-Rank Coal Samples

Pore Structure Characterization Using Mercury Intrusion Porosimetry

Figure 3 details the MIP measurement results. The hysteresis loops between the intrusion and withdraw curves of the middle-rank coal samples were wider than those of high-rank coal samples, which indicate that some of the intruded mercury was left in the pores. This may be due to the more developed open pores in the middle-rank coal samples, which are related to coalification degrees, material compositions, and molecular structures (Sun et al., 2020; Tao et al., 2018; Zhang et al., 2021). In addition, it is noticeable that the intrusion volumes of the sample BMG (middle-rank) and sample PB (high-rank) were larger and the hysteresis loops of the two samples were wider than those of the

other samples, indicating that the two samples may have developed more open pores as a result of different coal structures.

The total PVs of the middle- and high-rank coal samples ranged within 0.0240–0.0567 cm³/g and 0.0254–0.0553 cm³/g, respectively (Table 2). Figure 4 displays the PSD with a wide range of pore diameters, which demonstrates multi-peak characteristics. There was an abnormal sharp peak in sample XDA of high-rank coal ($\sim$ 30,000 nm), which may be attributed to the appearance of micro-fracture. However, it is difficult to determine whether microfracture is formed by sample preparation or under natural conditions (Guan et al., 2020). The middle-rank coal samples comprised mainly of transitional pores (29.75–49.30%) while the high-rank coal samples were composed predominately of micropores (36.52–63.76%). These indicate that transitional pores and micropores are more important for the evaluation of coal properties (Duan et al., 2021). The total SSA of the middle- and high-rank coal samples ranged within 5.221–7.462 m²/g and 12.238–21.694 m²/g, respectively (Table 2). In addition, the micropores (especially in high-rank coal samples) provided the majority of the SSA (Table 2, Fig. 4).

Pore Structure Characterization Using Low-Pressure N₂ Adsorption

Figure 5 shows the LPN₂A adsorption and desorption isotherms of the coal samples. According to the IUPAC classification, the samples can be divided into three types (Type A, Type B, and Type C) (Thommes et al., 2015). Type A had no obvious adsorption loops, indicating that the pores were mainly semi-open pores with one side closed (Figs. 5a, b). Different from Type A, Type C had obvious adsorption loops, and the hysteresis loops (H2) occurred in all samples (Sing, 1985). At the desorption branch, the hysteresis loops did not terminate at $P/P_0 = 0.5$, indicating that the pores of those samples were mainly in the shape of ink-bottle and parallel-plate (Cai et al., 2018). Type B is a transitional type and is more complex than those of the other two types, such as semi-open pores, ink-bottle pores, and slit-like pores (Zhang et al., 2019). Overall, the results imply that the samples developed a variety of pore types.

Table 3 shows the PV and SSA results of LPN₂A analysis. The total PV and SSA of the middle- and high-rank coal samples ranged within

Table 1. Basic experiment results of coal samples

| Coal Rank	Sample ID	R_o,max (%)	Macerals (%)				Proximate analysis (%)			
			Vitrinite	Inertinite	Exinite	Minerals	M_{ad}	A_d	V_{daf}	FC_d
Middle-rank coal	AX	1.25	68.6	22.1	–	9.3	0.77	14.38	22.58	66.29
	ZX	1.44	64.9	25.3	–	9.8	1.02	14.67	18.57	69.49
	TJ	1.14	66.6	24.9	2.7	5.9	0.92	8.74	27.72	65.97
	QY	1.27	65.6	21.5	–	12.9	1.09	19.19	23.55	61.78
	JX	1.15	66.1	25.7	2.8	5.5	1.12	8.41	24.69	68.98
	ALD	1.07	49.6	34.5	9.9	6.0	1.20	9.10	27.95	65.50
	BMG	1.04	65.9	30.0	–	4.1	0.80	6.34	25.14	70.11
	QPY	0.99	45.9	32.1	3.2	18.7	0.73	27.86	30.23	50.34
High-rank coal	DG	2.19	77.0	19.6	–	3.4	1.04	11.84	7.81	81.28
	DS	2.59	75.8	23.1	–	1.1	1.26	9.87	7.87	83.04
	HF	2.50	81.3	8.8	–	9.9	0.82	20.47	9.10	72.29
	PB	2.19	76.9	17.0	–	6.1	0.63	11.89	9.64	79.61
	SB	2.24	77.3	19.5	–	3.2	0.80	10.32	8.09	82.42
	SW	2.59	87.2	12.2	–	0.6	1.54	9.72	6.88	84.06
	XDO	2.29	72.5	13.2	–	14.3	0.80	32.82	13.72	57.96
	XDA	2.45	85.2	6.6	–	8.2	1.29	13.17	7.29	80.50
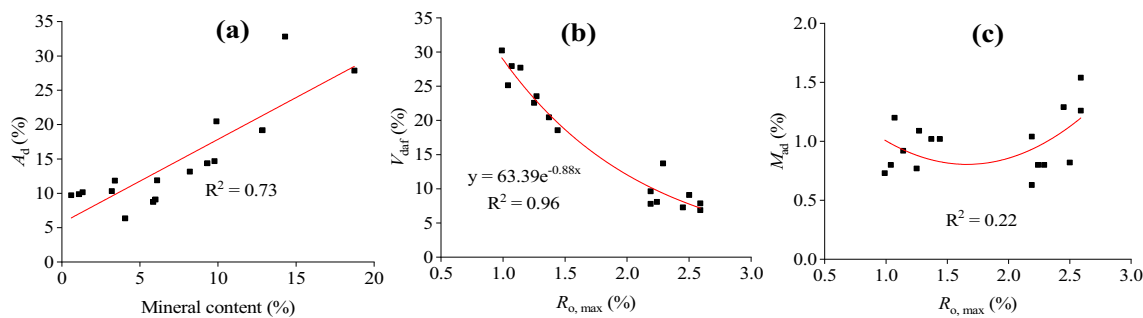
Figure 2. Relationships among proximate analysis parameters of middle- and high-rank coal samples.
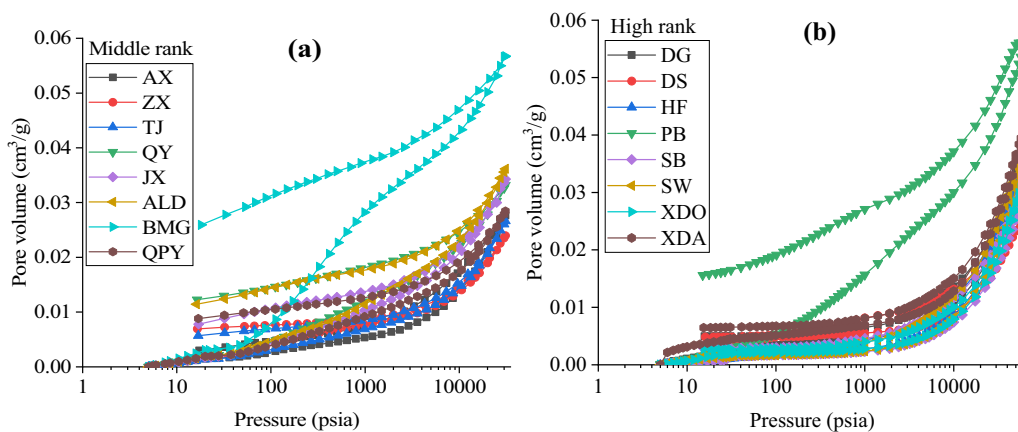

Figure 3. Intrusion and withdraw curves of coal samples: **a** middle-rank; **b** high-rank.

Table 2. Pore structural parameters of all the samples based on mercury intrusion porosimetry

| Coal Rank	Sample ID	V_{total} (cm³/g)	S_{total} (m²/g)	Percentage of pore volume (%)				Percentage of pore surface area (%)			
				Micropore	Transitional pore	Mesopore	Macropore	Micropore	Transitional pore	Mesopore	Macropore
Middle-rank coal	AX	0.0276	7.023	28.05	49.30	10.14	12.51	58.94	40.32	0.69	0.06
	ZX	0.0240	5.221	24.74	40.05	13.81	21.40	60.53	38.39	0.94	0.13
	TJ	0.0266	6.229	26.49	43.41	14.68	15.41	60.40	38.48	1.03	0.09
	QY	0.0332	5.898	19.01	38.93	22.94	19.12	57.31	40.48	2.04	0.16
	JX	0.0343	7.141	22.27	42.36	18.74	16.63	58.39	40.04	1.45	0.11
	ALD	0.0362	6.912	20.46	40.97	21.66	16.90	57.07	40.82	1.99	0.12
	BMG	0.0567	7.462	13.58	29.75	34.60	22.06	54.75	41.27	3.69	0.29
	QPY	0.0285	5.745	22.33	39.89	19.72	18.05	59.25	39.06	1.57	0.12
High-rank coal	DG	0.0369	20.962	59.48	26.73	4.08	9.72	89.91	9.95	0.14	0.01
	DS	0.0254	12.238	52.55	24.65	3.37	19.44	88.47	11.39	0.12	0.03
	HF	0.0340	19.615	60.97	29.06	4.23	5.74	89.21	10.64	0.14	0.01
	PB	0.0553	19.889	36.52	28.64	21.52	13.32	85.34	13.60	1.01	0.05
	SB	0.0293	17.025	61.05	29.41	3.48	6.06	89.18	10.69	0.13	0.01
	SW	0.0357	21.694	63.76	27.99	3.20	5.05	90.10	9.78	0.11	0.00
	XDO	0.0310	17.814	60.79	28.65	3.39	7.16	89.28	10.59	0.12	0.01
	XDA	0.0396	20.297	54.05	26.92	5.04	13.99	88.32	11.50	0.17	0.02
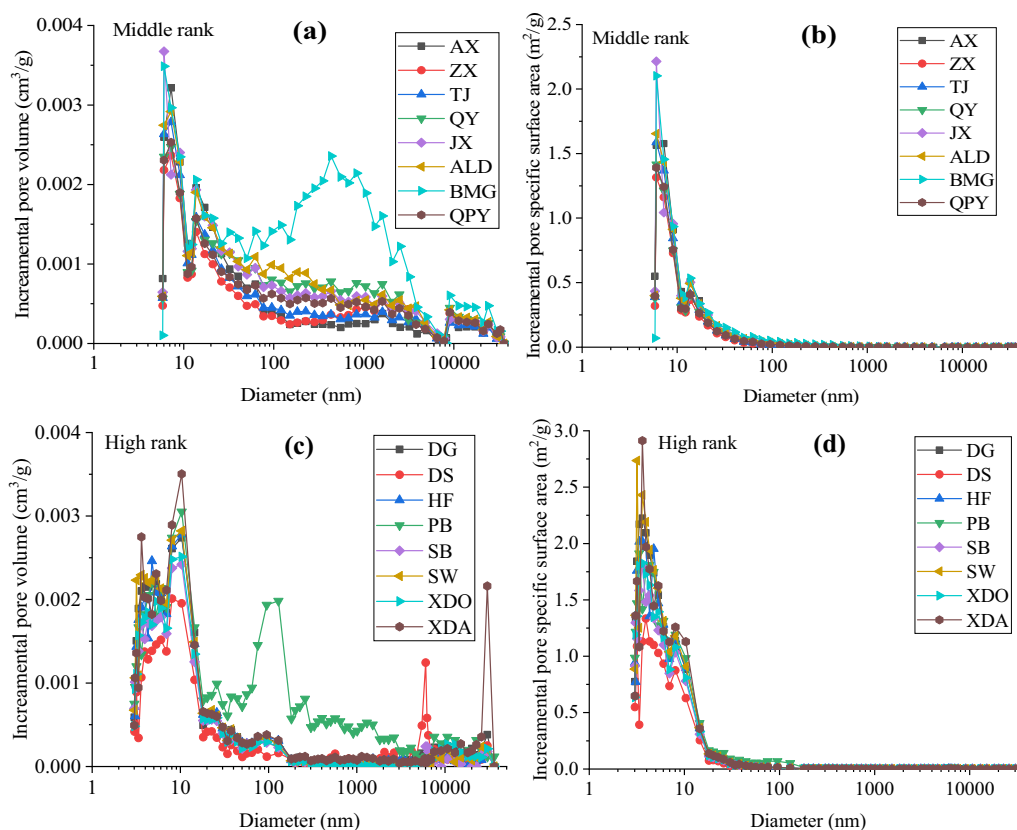
Figure 4. Distributions of incremental pore volumes and specific surface areas of coal samples: **a** and **b** middle-rank; **c** and **d** high-rank.

0.0012–0.0082 cm³/g and 0.202–3.281 m²/g, 0.0005–0.0049 cm³/g and 0.122–0.807 m²/g, respectively. The average pore sizes of the middle-rank coal samples ranged within 15.6–36.4 nm, which are much larger than those of the high-rank coal samples (8.45–25.1 nm). The PSDs in the three types are illustrated in Figure 6. Compared to the middle-rank coal samples, micropores in the high-rank coal samples were more developed, and their PV showed an obvious multiple-peaked distribution.

Multifractal Characteristics

Multifractal Features from Mercury Intrusion Porosimetry

Figure 7 shows two selected plots of double logarithm curves for the partition function $\chi(q,\varepsilon)$ vs. the box scale ε with the worst linear correlation. The statistical moment order was $q = -10$ to 10 with

the interval order $q = 1$. There was good linear relationship between log $\chi(q,\varepsilon)$ and $\log_\varepsilon$ for all the middle- and high-rank coal samples with coefficients larger than 0.98 and 0.93, respectively (Fig. 7). This indicates that the PSDs of the samples display multifractal features (Muller, 1996). In addition, the convex features of the relationship of the quality index $\tau(q)$ and q further confirms that the PSDs of the samples show multifractal characteristics (Fig. 8).

D_q represents the generalized fractal dimensions; when $q = 0$, 1, 2, D_q represents capacity dimension, information dimension, and correlation dimension, respectively (Posadas et al., 2001). The capacity dimension D_0 refers to the scaling characteristic of the number of nonempty boxes in different scales. The information dimension D_1 provides the information of the concentration degree of the PSD, and the correlation dimension D_2 computes the uniformity among the measures.
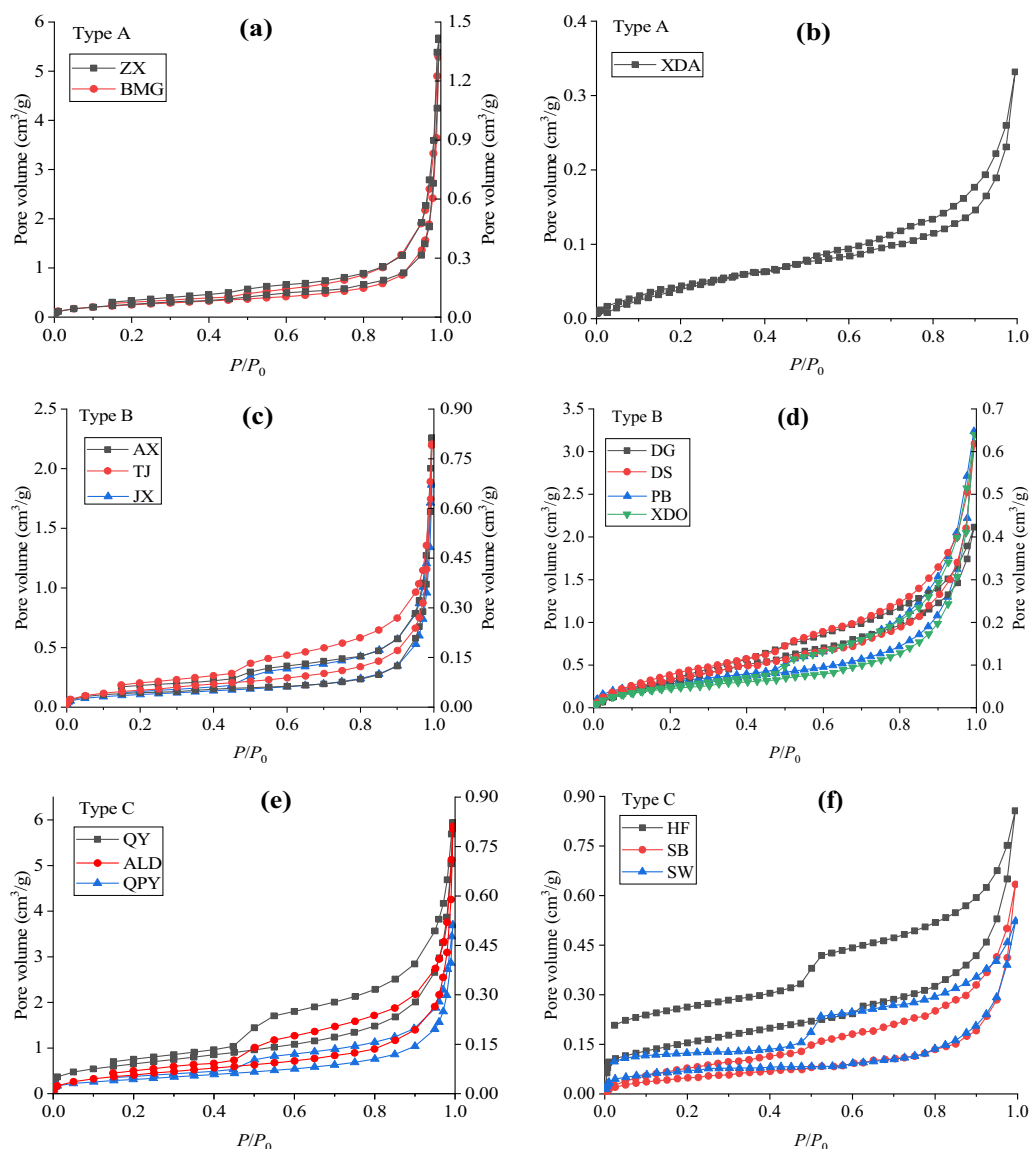
Figure 5. Low-temperature nitrogen adsorption and desorption isotherms of all samples: **a**, **c**, and **e** middle-rank; **b**, **d**, and **f** high-rank.

Figure 9 shows the curves of D_q in the range of $-10 \leq q \leq 10$ for successive 0.01 steps, which revealed a monotonic decrease feature with increase in q. Moreover, D_q decreased sharply ($q < 0$) and the tendency became flat ($q > 0$), particularly in the middle-rank coals. Table 4 lists the related parameters of D_q. In this paper, $D_0 = 1$ for all samples indicated that $D_0 > D_1 > D_2$, proving that the pore structures of all samples had multifractal characteristics (Posadas et al., 2001). In addition, the information dimension D_1 indicates the heterogeneity

changes in a distribution, with smaller D_1 representing lower uniformity of PSD (Ferreiro et al., 2009; Vázquez et al., 2008). In this study, the D_1 values ranged from 0.9219 to 0.9639 and from 0.6863 to 0.9071 for the middle- and high-rank coals, respectively. This phenomenon suggests that irregularities in the high-rank coals were more concentrated than those in the middle-rank coals. D_2 values ranged from 0.8896 to 0.9413 and from 0.5309 to 0.8301 for the middle- and high-rank coals, respec-

Table 3. Pore structural parameters of all the samples based on low-pressure N_2 adsorption

Coal Rank	Sample ID	V_{total} cm^3/g	S_{total} m^2/g	D_N (nm)	Percentage of pore volume (%)			Percentage of pore surface area (%)		
					Micropore	Transitional pore	Mesopore	Micropore	Transitional pore	Mesopore
Middle rank	AX	0.0012	0.202	36.4	12.58	55.41	32.01	64.68	30.79	4.53
	ZX	0.0022	0.285	35.4	8.64	58.70	32.67	51.95	32.11	15.94
	TJ	0.0012	0.272	25.7	21.00	48.22	30.78	74.40	22.60	3.00
	QY	0.0094	3.281	15.6	34.04	48.50	17.46	81.89	17.02	1.08
	JX	0.0030	0.645	30.4	18.60	52.59	28.81	71.95	25.12	2.93
	ALD	0.0013	0.346	23.0	25.85	43.31	30.84	79.72	18.09	2.19
	BMG	0.0082	1.087	35.6	9.68	59.45	30.87	49.62	45.13	5.25
	QPY	0.0058	1.590	19.9	25.86	51.45	22.69	77.59	20.76	1.65
High rank	DG	0.0006	0.229	8.45	41.50	50.62	7.88	78.65	20.54	0.81
	DS	0.0009	0.208	13.1	42.56	38.72	18.73	65.23	33.18	1.59
	HF	0.0012	0.297	9.61	43.67	38.53	17.80	67.23	31.53	1.25
	PB	0.0049	0.807	19.5	47.51	32.99	19.50	48.06	49.48	2.46
	SB	0.0010	0.156	20.2	34.20	40.67	25.13	54.07	43.71	2.22
	SW	0.0008	0.126	13.0	51.58	27.71	20.71	42.26	56.28	1.47
	XDO	0.0010	0.145	25.1	46.00	29.27	24.73	44.58	53.04	2.38
	XDA	0.0005	0.122	10.8	37.96	37.87	24.17	71.52	26.93	1.55

V_{total}, total pore volume, cm^3/g; S_{total}, total pore specific surface area, m^2/g; D_N, adsorption average pore width (4 V/A by BET), nm

tively; D_2 values of high-rank coals were lower than those of middle-rank coals.

The H values (also known as long-range correlation index) can be used to describe the correlation degrees of the local porosity distributions. The H values of the middle- and high-rank coal samples were in the ranges of 0.9448–0.9707 (average 0.9628) and 0.7655–0.91550 (average 0.7979), respectively. The closer the H values are to 1, the more connectivity of pore structures exists. The generalized dimension D_q is more useful for the comprehensive study of multifractals. The spectrum width $D_{-10} - D_{10}$, the left branch $D_{-10} - D_0$, and the right branch $D_0 - D_{10}$ were also assessed. The spectra of high-rank coal samples were wider than those of the middle-rank coal samples, indicating that the high-rank coals had higher PSD heterogeneity. The $D_{-10} - D_0$ values were greater than those of the $D_0 - D_{10}$, which suggest that the heterogeneity of low value areas of PV was more obvious than that of high value areas of PV.

Figure 10 shows the multifractal singularity spectra $f(\alpha)$ in the shape of asymmetric concave parabolic. The differences between $f(\alpha)$ spectra shapes for the middle- and high-rank coals manifest that the smaller pores responsible for most of the PV and SSA were more frequent in the high-rank coal

samples, while the larger pores were more frequent in the middle-rank coal samples (Ferreiro et al., 2009). This is consistent with the PSD results discussed above. α_0 represents the average of the singularity strength of the PSD. The higher α_0 indicates that the distribution range is narrower and the heterogeneity is much stronger. The widths of the $f(\alpha)$ spectra $\alpha_{10-} - \alpha_{10+}$ ranged within 0.6389–1.0832 and 0.9708–1.7671 for the middle- and high-rank coals, respectively (Table 4). A greater $\alpha_{10-} - \alpha_{10+}$ value indicates a complex pore structure (Duan et al., 2021; Guan et al., 2020). The width differences of the left and right branches $R_d = [(\alpha_{10-} - \alpha_0) - (\alpha_0 - \alpha_{10+})]$ indicate the deviation degrees of spectrum from the center. If $R_d > 0$, the $f(\alpha)$ spectrum deviates to the left, and the PSD is dominantly influenced by the effects of the dense area. In contrast, the PSD is affected by sparse area (Liu et al., 2018a; Yu et al., 2018; Zhang et al., 2021). In this study, the R_d values of the middle-rank samples were all negative, meaning that the effect of larger pores was dominant, whereas the pore structure of high-rank coal samples was affected mainly by smaller pores. Overall, the high-rank coal samples were more heterogeneous than middle-rank coal samples.
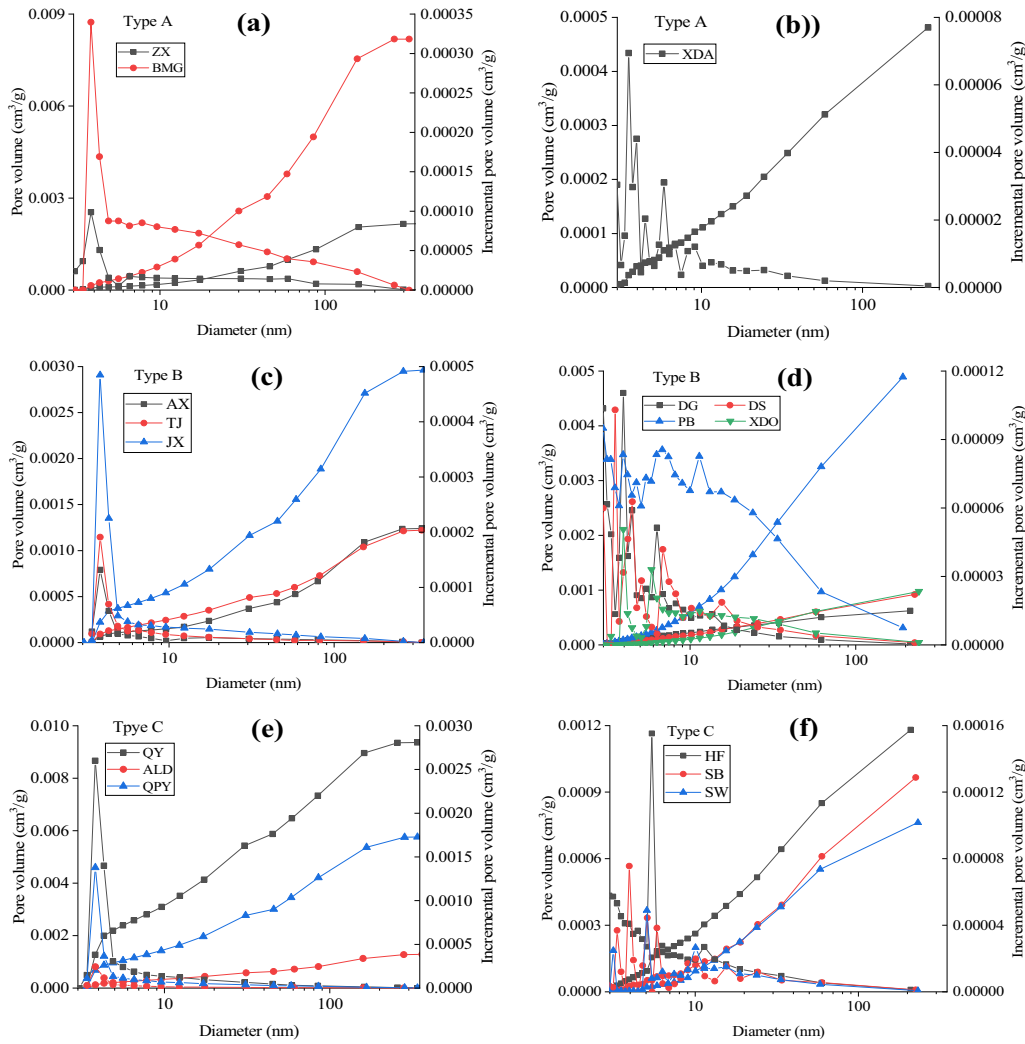
Figure 6. Cumulative pore volumes and pore size distributions from low-pressure N_2 adsorption.

Multifractal Features from Low-Pressure N_2 Adsorption

Figure 11 shows two log–log plots with the worst correlation from LPN$_2$A method. The successive regression lines in the range of $0 < q \leq 10$ from LPN$_2$A method were closer than that from the MIP method, suggesting that most of the measure concentrated on a small area of the scale measured by LPN$_2$A (Ferreiro et al., 2009). In addition, the convex feature of the relationship of $\tau(q)$ and q indicates that the PSD exhibits multifractal characteristics (Fig. 12). The generalized dimension curves and singularity spectra are displayed in Figures 13 and 14; similarly, the characteristics of the two kinds

of curves from LPN$_2$A follow a self-similarity pattern.

The information dimension D_1 values from LPN$_2$A varied within the ranges of 0.7345–0.9064 and 0.5679–0.8372 for the middle- and high-rank coals (Table 5), which were all lower than those from the MIP method. This means that the PSD from LPN$_2$A was less uniform compared to that from MIP. The H values of the middle- and high-rank coal samples from LPN$_2$A were in the ranges of 0.7998–0.9180 (average 0.8666) and 0.6956–0.8473 (average 0.7603), respectively. The wider spectra indicated by $D_{-10} - D_{10}$ and $\alpha_{10-} - \alpha_{10+}$ imply that the PSD from LPN$_2$A was more heterogeneous, and the pore structures were more complex. The R_d
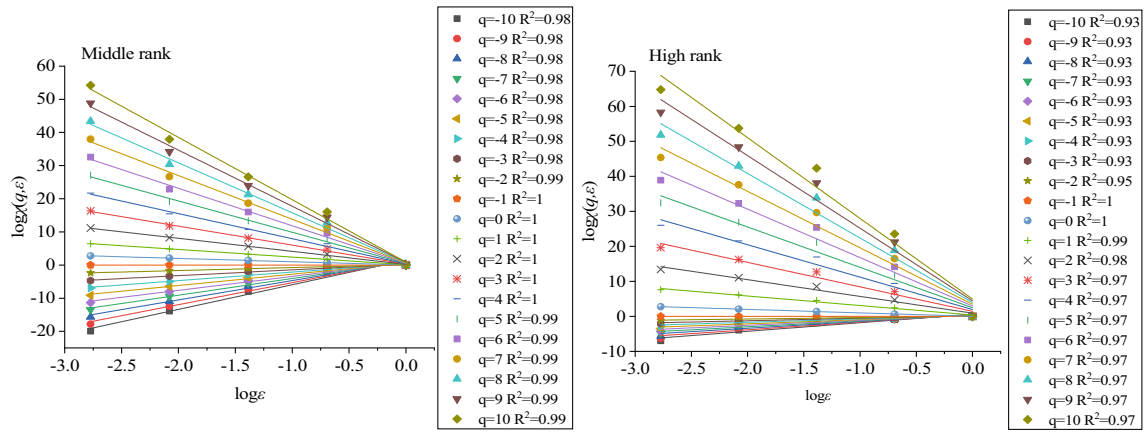
Figure 7. Double logarithm curves of partition function vs. box scale with the worst correlation from the MIP method.
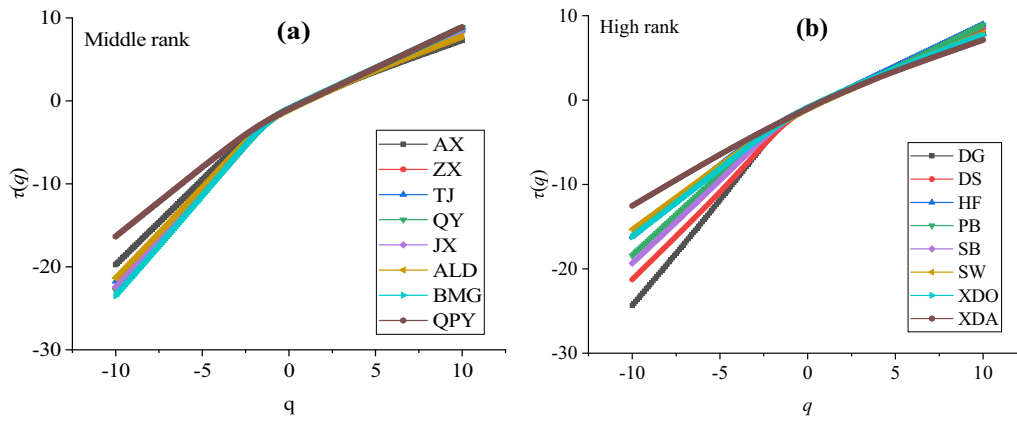

Figure 8. Mass scaling function $\tau(q)$ of different rank coals from the MIP method.
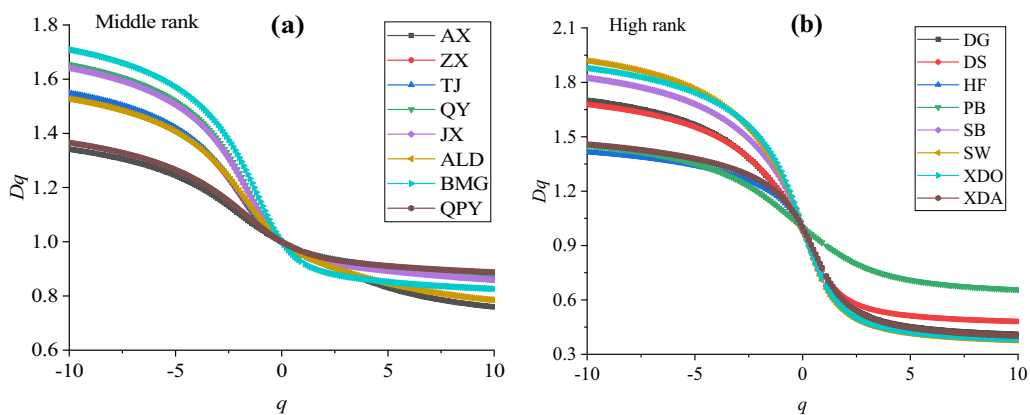

Figure 9. Generalized dimension Dq vs. q of different rank coals from the MIP method.

Table 4. Multifractal parameters of middle- and high-rank coal samples from the MIP method porosimetry

Rank	Sample ID	H	D_1	D_2	$D_{-10} - D_{10}$	$D_{-10} - D_0$	$D_0 - D_{10}$	α_0	$\alpha_{10-} - \alpha_{10+}$	R_d
Middle-rank coal	AX	0.9621	0.9610	0.9241	0.5819	0.3415	0.2404	1.0424	0.7776	− 0.0692
	ZX	0.9704	0.9639	0.9408	0.6674	0.5457	0.1217	1.0494	0.8546	− 0.4485
	TJ	0.9705	0.9631	0.9410	0.6809	0.5479	0.1330	1.0516	0.8890	− 0.4127
	QY	0.9625	0.9491	0.9250	0.7703	0.6542	0.1161	1.0747	0.9550	− 0.5347
	JX	0.9638	0.9520	0.9276	0.7821	0.6418	0.1403	1.0693	0.9935	− 0.4795
	ALD	0.9574	0.9495	0.9148	0.7427	0.5272	0.2155	1.0649	0.9608	− 0.2629
	BMG	0.9448	0.9219	0.8896	0.8836	0.7099	0.1737	1.1139	1.0832	− 0.4445
	QPY	0.9707	0.9635	0.9413	0.4780	0.3655	0.1125	1.0460	0.6389	− 0.2583
High-rank coal	DG	0.7937	0.7537	0.5874	1.2906	0.7012	0.5894	1.2283	1.4951	0.2154
	DS	0.8044	0.7384	0.6087	1.1974	0.6786	0.5188	1.2221	1.3808	0.1590
	HF	0.7696	0.7146	0.5392	1.0270	0.4156	0.6114	1.2338	1.1543	0.5865
	PB	0.9150	0.9071	0.8301	0.7952	0.4525	0.3427	1.0972	0.9708	0.0019
	SB	0.7704	0.6971	0.5408	1.4442	0.8247	0.6195	1.3255	1.6578	0.3028
	SW	0.7655	0.6863	0.5309	1.5417	0.9193	0.6224	1.3454	1.7671	0.2364
	XDO	0.7720	0.6965	0.5440	1.4964	0.8794	0.6170	1.3539	1.7005	0.3119
	XDA	0.7927	0.7531	0.5855	1.0573	0.4584	0.5989	1.2251	1.2086	0.5170
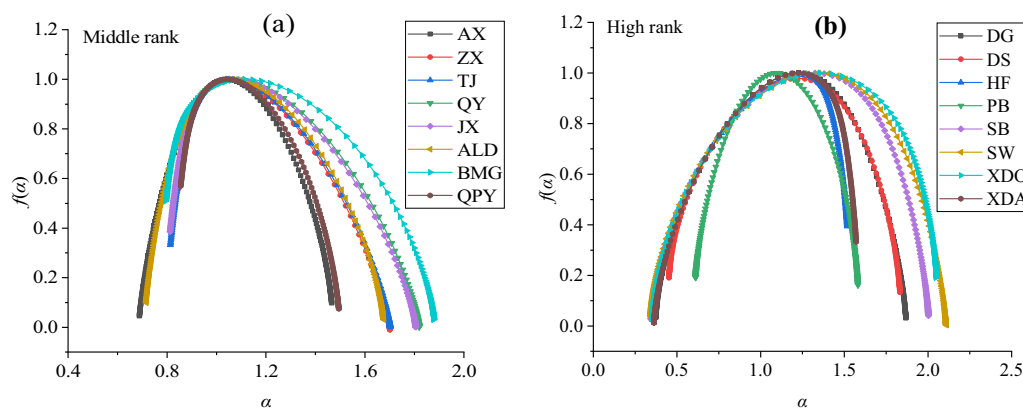
Figure 10. Multifractal singularity spectra $f(\alpha)$ vs. α of different rank coals from the MIP method.

values of all samples were positive (except sample ZX with R_d value of − 0.0215) in the pore throat measured by LPN$_2$A, implying that the dense area of porosity distribution was dominant in these samples.

DISCUSSION

Comparison of Pore Structure Heterogeneity with Different Methods

The pore structure heterogeneities derived from the MIP and LPN$_2$A methods were different due to the inconsistencies in the detection ranges. There were no significant correlations observed between multifractal parameters from the MIP and LPN$_2$A results (Fig. 15). However, the pore structure heterogeneity of LPN$_2$A was much stronger than that from MIP. This can be attributed to the significant contribution of smaller pores (pore sizes of < 10 nm) and the limited number of larger pores (pore diameters of > 350 nm). Compared to the MIP method, the LPN$_2$A method had a narrower detecting pore size range. As a result, the undetectable pore size range larger than 350 nm may potentially result in inaccurate evaluations of the degree of pore structure heterogeneity, and the large amount of pores with small aperture sizes could potentially increase the degree of heterogeneity. Therefore, a combination of the two methods allows
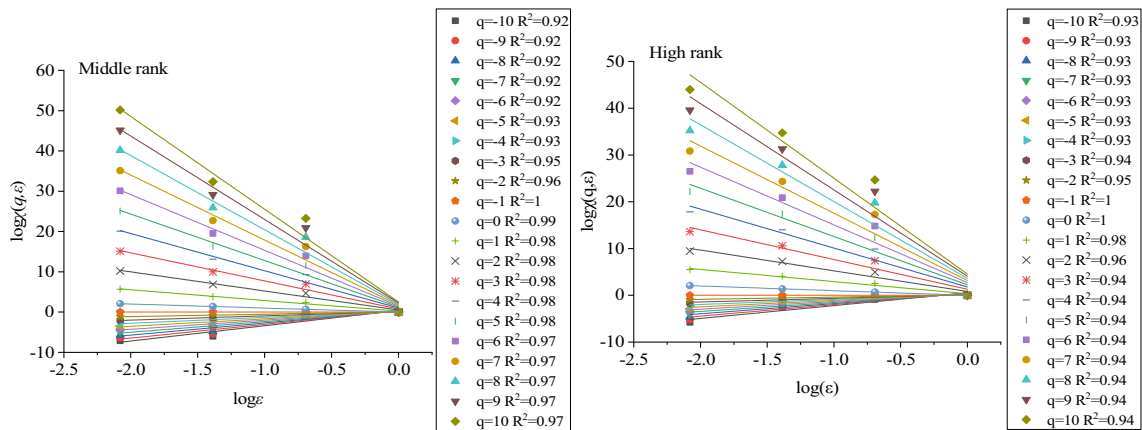
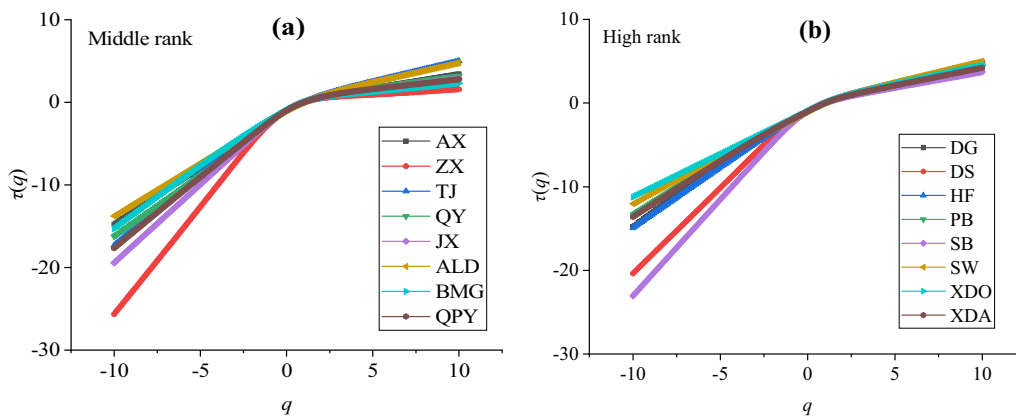**Figure 11.** Double logarithm curves of partition function vs. the box scale with the worst correlation from the LPN$_2$A method.

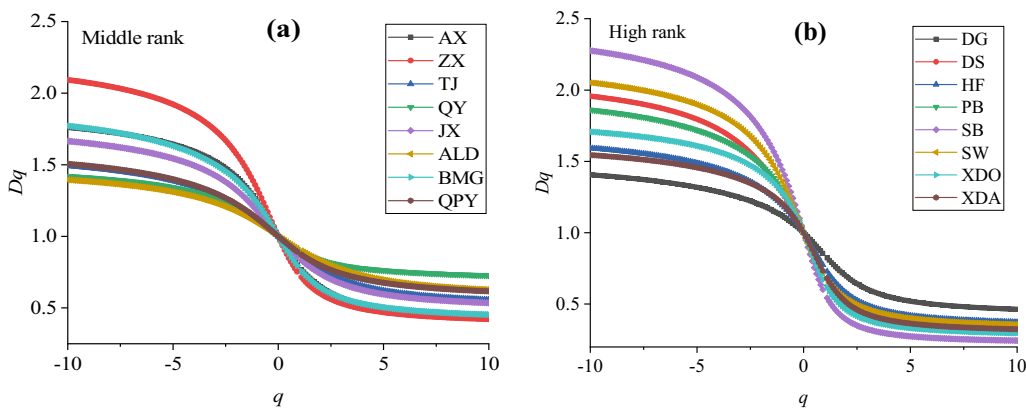**Figure 12.** Mass scaling function $\tau(q)$ of different rank coals from the LPN$_2$A method.

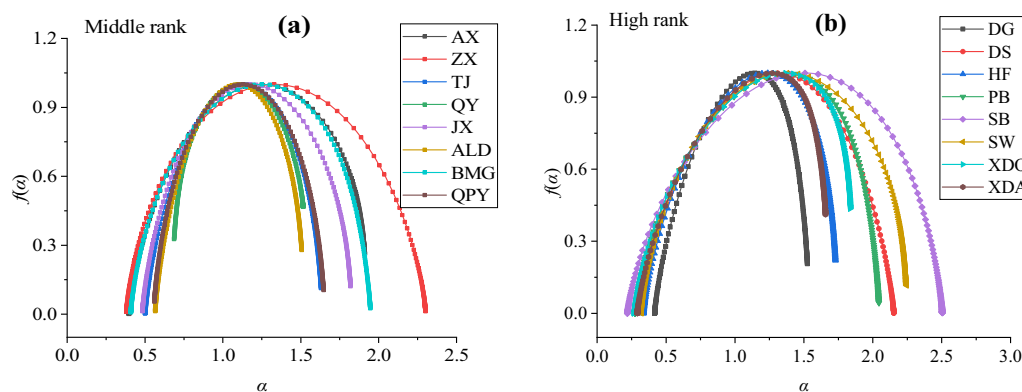**Figure 13.** Generalized dimension Dq vs. q of different rank coals from the LPN$_2$A method.

Figure 14. Multifractal singularity spectra $f(\alpha)$ vs. α of different rank coals from the LPN_2A method.

Table 5. Multifractal parameters of middle- and high-rank coal samples from the LPN_2A method

Rank	Sample ID	H	D_1	D_2	$D_{-10} - D_{10}$	$D_{-10} - D_0$	$D_0 - D_{10}$	α_0	$\alpha_{10-} - \alpha_{10+}$	R_d
Middle-rank coal	AX	0.8241	0.7835	0.6481	1.3202	0.7614	0.5588	1.2502	1.5141	0.1918
	ZX	0.7998	0.7345	0.5995	1.6714	1.0928	0.5786	1.3298	1.9204	− 0.0215
	TJ	0.8863	0.8746	0.7726	0.9357	0.4922	0.4435	1.1281	1.1289	0.1250
	QY	0.9180	0.9000	0.8359	0.6930	0.4200	0.2731	1.1116	0.8283	0.0211
	JX	0.8695	0.8453	0.7391	1.1299	0.6654	0.4645	1.1751	1.3364	0.0472
	ALD	0.9141	0.9064	0.8282	0.7676	0.3942	0.3734	1.0968	0.9404	0.1225
	BMG	0.8222	0.7759	0.6445	1.3185	0.7720	0.5465	1.2508	1.5376	0.1459
	QPY	0.8985	0.8829	0.7971	0.8904	0.5065	0.3839	1.1268	1.0867	0.0469
High-rank coal	DG	0.8473	0.8387	0.6945	0.9427	0.4063	0.5364	1.1439	1.1090	0.3444
	DS	0.7596	0.7012	0.5192	1.6287	0.9576	0.6711	1.3098	1.8573	0.1703
	HF	0.7883	0.7521	0.5767	1.2194	0.5927	0.6266	1.2383	1.3940	0.4105
	PB	0.7358	0.6486	0.4715	1.5578	0.8625	0.6953	1.3753	1.7702	0.4320
	SB	0.6956	0.5679	0.3911	2.0330	1.2771	0.7559	1.5083	2.2849	0.2922
	SW	0.7683	0.6902	0.5365	1.6954	1.0519	0.6435	1.3780	1.9245	0.1896
	XDO	0.7308	0.6435	0.4616	1.4123	0.7088	0.7035	1.3667	1.5692	0.6304
	XDA	0.7565	0.7063	0.5130	1.2208	0.5448	0.6760	1.2702	1.3666	0.5906

to characterize more accurately the pore structures and structural heterogeneity of the coal samples.

Relationship of Pore Structures and Multifractal Parameters

Figure 16 demonstrates the correlations among H, $D_{-10} - D_{10}$, $\alpha_{10-} - \alpha_{10+}$, R_d, total PV, and total SSA. For the intervals of pore diameters measured by the MIP method, total PV hardly affected the pore connectivity, pore structures, and degree of heterogeneity of the PSD, while the total SSA had a relatively high impact on pore heterogeneity (Figs. 16a, c, e, g). The H value decreased with increase in total SSA (Fig. 16a), indicating that in-

creases in total SSA weakened pore connectivity. Increases in total SSA enhanced the complexity of pore structures and heterogeneity (Figs. 16c, e, g). However, for pores between 3 and 350 nm measured by the LPN_2A method, the heterogeneities of pore structures and pore connectivity were hardly influenced by total PV and total SSA (Figs. 16b, d, f, h).

The micropores measured by the MIP method had the most significant influences on the multifractal parameters of the pore structures (Table 6). The micropores were negatively correlated with H ($R^2 = 0.944$), and positively correlated with $D_{-10} - D_{10}$, $\alpha_{10-} - \alpha_{10+}$, and R_d ($R^2 = 0.744$, 0.697 and 0.849, respectively), indicating that increases of micropores made the pore structure more complex and the pore connectivity became worse, thereby affecting the
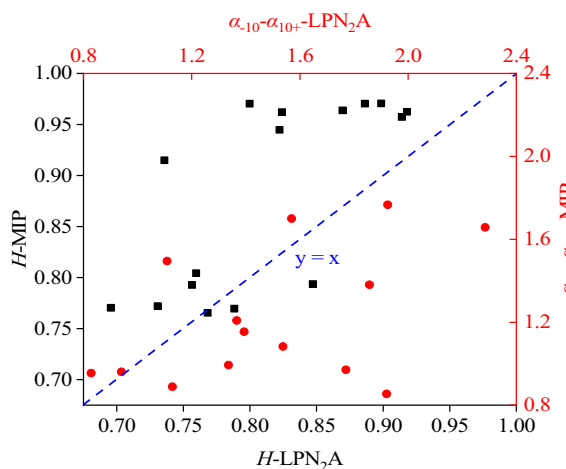
Figure 15. Comparison of pore structure heterogeneity from MIP and LPN$_2$A methods.

heterogeneity of the pore structures. The influencing effects of transitional pores, mesopores, and macropores on the multifractal parameters were opposite to those of micropores (Table 6). The transitional pores, mesopores, and macropores were positively correlated with H, and negatively correlated with $D_{-10} - D_{10}$, $\alpha_{10-} - \alpha_{10+}$ and R_d. These results indicate that increases in transitional pores, mesopores, and macropores tended to improve pore connectivity and weaken the complexity of pore structures, thereby reducing the heterogeneity of the pore structures.

The relationships between the pores measured by the LPN$_2$A and the multifractal parameters were relatively weak. Among those relationships, the transitional pores had the greatest influences on multifractal characteristics of the pore structures. The increases in transitional pores may have potentially enhanced the connectivity of pores and decreased the heterogeneity of the pore structures. There was little correlation between mesopores and multifractal parameters. This may be related to the limited measurement scale of the LPN$_2$A. Similar to the MIP results, the micropores also displayed negative effects on H and positive effects on $D_{-10} - D_{10}$, $\alpha_{10-} - \alpha_{10+}$, and R_d. Overall, the development of the micropores was detrimental to the connectivity and homogeneity of the pore structures. Therefore, this study considers that micropores were the most important features affecting the connectivity of pores in middle- to high-rank coals and may even

have a negative impact on gas seepage during the process of exploitation.

Relationship of Coal Rank and Multifractal Parameters

With increasing coalification degree, the H values measured by the MIP and LPN$_2$A methods decreased, while $D_{-10} - D_{10}$, $\alpha_{10-} - \alpha_{10+}$, and R_d increased (Fig. 17). For the middle- to high-rank coals, coal structures would become better orientated and the coal bulk further compacted as the maturity increased due to the strength of coal macromolecular polycondensation effect, leading to the decreasing number of mesopores and the formation of smaller pores (Liu & He, 2017; Liu et al., 2018a, 2018b, 2018c; Mathews & Sharma, 2012; Nie et al., 2015). As discussed above, the micropores had negative impacts on the heterogeneity of the pore structures. Consequently, the pore connectivity decreased, and the pore structures became more complex. In addition, the uniformity of the PSD reduced during the process of coalification. However, the correlation coefficients between $R_{o,max}$ and the multifractal parameters derived from the LPN$_2$A were lower than those from the MIP, especially for the parameters of $D_{-10} - D_{10}$ and $\alpha_{10-} - \alpha_{10+}$. These results can be explained as due to the difference of pore size scale and the PSD measured by the different methods. In LPN$_2$A measurement, the PSDs of most coal samples were multimodal, and so the heterogeneity of the PSDs was affected by multiple peaks.

Relationship of Coal Maceral Composition, Proximate Analysis, and Multifractal Parameters

The vitrinite and inertinite contents showed negative and positive trends with the Hurst exponent H, with coefficients of 0.593 and 0.572 for the MIP method, and 0.521 and 0.415 for the LPN$_2$A method, respectively. Therefore, increases in vitrinite content could potentially decrease the connectivity of pore structures, while increases in inertinite content have an opposite effect. The correlations of vitrinite and inertinite contents with $D_{10} - D_{10}$, $\alpha_{10-} - \alpha_{10+}$, and R_d were also opposite. However, the correlations of inertinite content with ($D_{-10} - D_{10}$ and $\alpha_{10-} - \alpha_{10+}$ from the LPN$_2$A were not obvious. This indicates that the effects of the
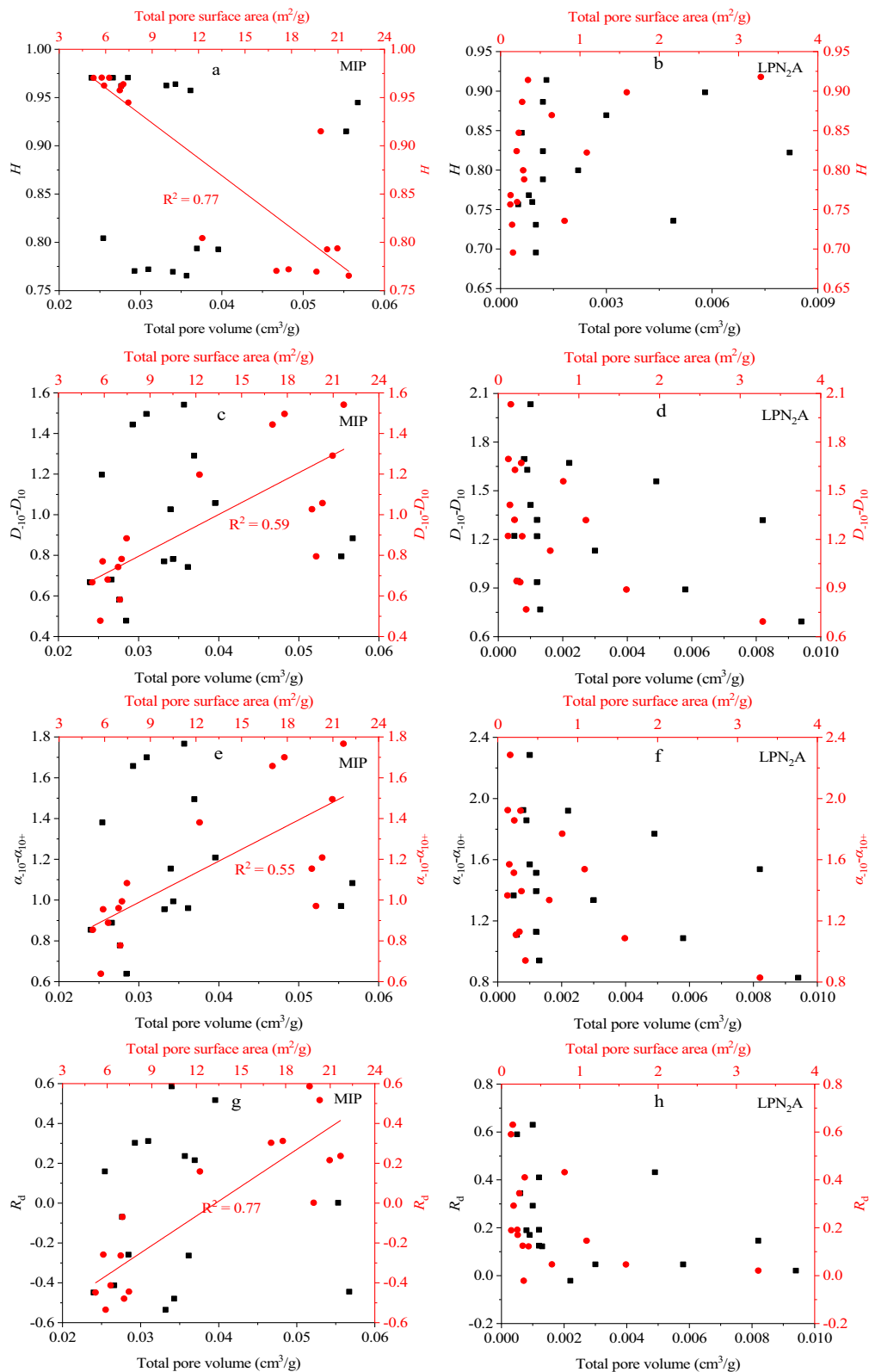
Figure 16. Relationships of pore structures and multifractal parameters.

Table 6. Relationships of pore structures and multifractal parameters

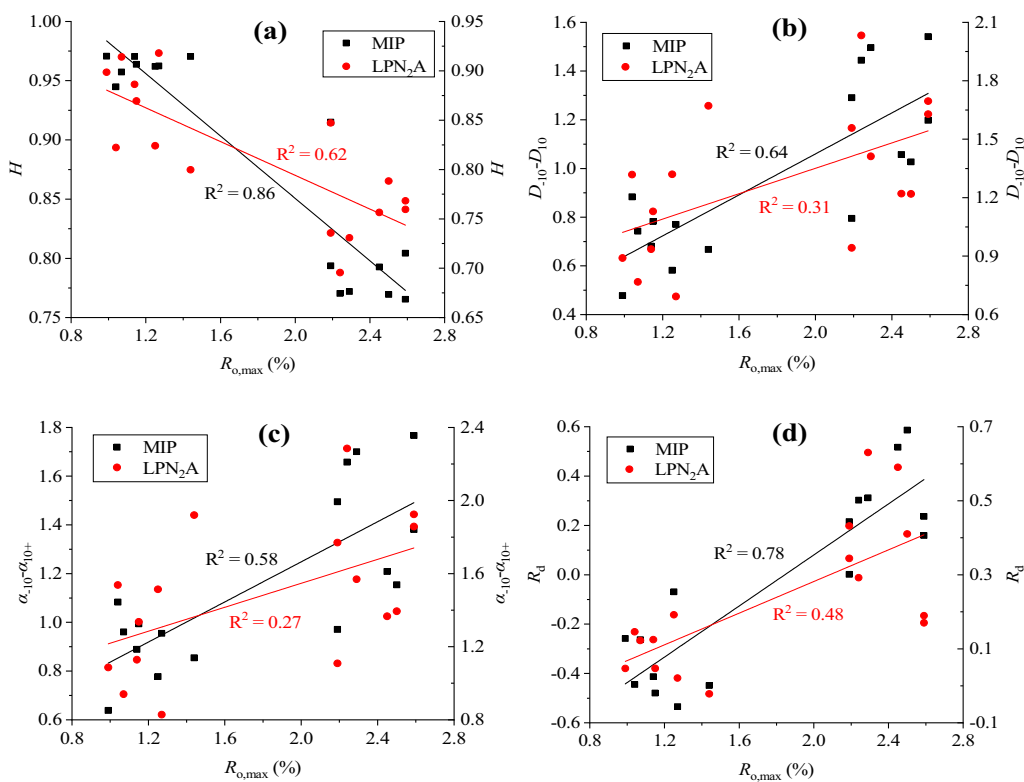| Parameter		H	$D_{-10} - D_{10}$	$\alpha_{10-} - \alpha_{10+}$	R_d
MIP	Micropore	− 0.944	0.744	0.697	0.849
	Transitional pore	0.669	− 0.590	− 0.541	− 0.470
	Mesopore	0.643	− 0.446	− 0.418	− 0.639
	Macropore	0.567	− 0.471	− 0.454	− 0.591
LPN$_2$A	Micropore	− 0.219	0.034	0.023	0.391
	Transitional pore	0.333	− 0.110	− 0.089	− 0.429
	Mesopore	0.015	0.011	0.016	− 0.111
	Macropore	–	–	–	–

Figure 17. Impacts of coal ranks on pore connectivity and heterogeneity.

inertinite contents on multifractal parameters were more obvious in the larger ranges of pores. There was little or no correlation between minerals and multifractal parameters, especially for the results from the LPN$_2$A. Thus, the effects of mineral content on multifractal parameters can be neglected.

In addition, no obvious correlations were found between the multifractal parameters and M_{ad}, A_d for both methods (Table 7). At the confidence interval

of $p = 0.01$, there were strong correlations between V_{daf} and multifractal parameters. However, the correlation coefficients for LPN$_2$A method were lower than those for the MIP method (Table 7). The positive correlations between V_{daf} and H values meant that increases in V_{daf} could potentially enhance correlations of pore groups in segments with different sizes, thereby enhancing pore connectivity. It also indicates that the coalification degrees have

Table 7. Relationships of maceral compositions, proximate analysis, and multifractal parameters

Variables	MIP				LPN$_2$A			
	H	$D_{-10} - D_{10}$	$\alpha_{10-} - \alpha_{10+}$	R_d	H	$D_{-10} - D_{10}$	$\alpha_{10-} - \alpha_{10+}$	R_d
V	− 0.593	0.492	0.458	0.506	− 0.521	0.297	0.263	0.364
I	0.572	− 0.353	− 0.305	− 0.635	0.415	− 0.119	− 0.090	− 0.575
Mineral	0.102	− 0.203	− 0.227	− 0.025	0.092	− 0.178	− 0.188	0
M_{ad}	− 0.067	0.115	0.124	0.009	0.008	− 0.001	− 0.001	− 0.023
A_d	− 0.019	0.001	0	0.047	− 0.001	− 0.028	− 0.038	0.097
V_{daf}	0.776	− 0599	− 0.551	− 0.695	0.647	− 0.347	− 0.337	− 0.422

significant impacts on coal multifractal characteristics, which is consistent with the discussion above.

CONCLUSIONS

To examine the multifractal characteristics of middle- and high-rank coal, mercury injection porosimetry (MIP) and low-pressure N$_2$ adsorption (LPN$_2$A) experiments were conducted on 16 middle- and high-rank coal samples. The relationships of the multifractal parameters and physical properties were also discussed. The conclusions are as follows.

(1) The multifractal parameters derived from the MIP and LPN$_2$A methods were different and had no significant correlations. The pore structure heterogeneity calculated from the LPN$_2$A method was much stronger than that from the MIP method.

(2) There were no obvious impacts of total pore volume (PV) on multifractal parameters measured by both methods. However, the total specific surface area (SSA) obtained from the MIP method had a relatively high impact on pore heterogeneity. The development of micropores was detrimental to the connectivity and homogeneity of the pore structures. The influencing effects of the transitional pores, mesopores, and macropores measured by the MIP method on the multifractal characteristics were opposite to those of the micropores. The relationships of pores measured by the LPN$_2$A method and the multifractal parameters were relatively weak. However, increases in the number of transitional pores could potentially improve pore connectivity.

(3) The heterogeneity and complexity of the pore structures increased with increase in coalification degree. In addition, the correlation coefficients between the coalification degrees and the multifractal parameters derived from the LPN$_2$A method were lower than those from MIP method.

(4) The correlations of vitrinite and inertinite contents with multifractal parameters were opposite. Increases in vitrinite content could potentially decrease the connectivity of the pore structures, while increases in inertinite content have an opposite effect. In addition, there were no obvious correlations among the multifractal parameters and minerals, moisture content and dry base ash for both methods.

REFERENCES

Blach, T., Radlinski, A. P., Edwards, D. S., Boreham, C. J., & Gilbert, E. P. (2020). Pore anisotropy in unconventional hydrocarbon source rocks: A small-angle neutron scattering (SANS) study on the Arthur Creek Formation, Georgina Basin, Australia. *International Journal of Coal Geology, 225*, 103495.

Cai, Y., Li, Q., Liu, D., Zhou, Y., & Lv, D. (2018). Insights into matrix compressibility of coals by mercury intrusion porosimetry and N2 adsorption. *International Journal of Coal Geology, 200*, 199–212.

Chen, S., Tang, D., Tao, S., Ji, X., & Xu, H. (2019). Fractal analysis of the dynamic variation in pore-fracture systems under the action of stress using a low-field NMR relaxation method: An experimental study of coals from western Guizhou in China. *Journal of Petroleum Science and Engineering, 173*, 617–629.

Cheng, G., Jiang, B., Li, M., Li, F., & Xu, S. (2020). Quantitative characterization of fracture structure in coal based on image processing and multifractal theory. *International Journal of Coal Geology, 228*, 103566.

Clarkson, C. R., & Bustin, R. M. (1999). The effect of pore structure and gas pressure upon the transport properties of coal a laboratory and modeling study. 1. *Isotherms and Pore Volume Distributions. Fuel, 78*, 1333–2134.

Davis, K. J., & Gerlach, R. (2018). Transition of biogenic coal-to-methane conversion from the laboratory to the field: A review of important parameters and studies. *International Journal of Coal Geology, 185*, 33–43.

Duan, R., Xu, Z., Dong, Y., & Liu, W. (2021). Characterization and classification of pore structures in deeply buried carbonate rocks based on mono- and multifractal methods. *Journal of Petroleum Science and Engineering, 203*, 108606.

Ferreiro, J. P., Wilson, M., & Vázquez, E. V. (2009). Multifractal description of nitrogen adsorption isotherms. *Vadose Zone Journal, 8*, 209–219.

Gao, L., Mastalerz, M., & Schimmelmann, A. (2020). 1a - The origin of coalbed methane. *Coal Bed Methane (second Edition)*. https://doi.org/10.1016/B978-0-12-815997-2.00001-9.

Guan, M., Liu, X., Jin, Z., & Lai, J. (2020). The heterogeneity of pore structure in lacustrine shales: Insights from multifractal analysis using N2 adsorption and mercury intrusion. *Marine and Petroleum Geology, 114*, 104150.

Hodot, B. B. (1961). *Outburst of coal and coalbed gas*. National Mining Scientific and Technical Documentation Press.

Ju, W., Yang, Z., Qin, Y., Yi, T., & Zhang, Z. (2018). Characteristics of in-situ stress state and prediction of the permeability in the upper Permian coalbed methane reservoir, western Guizhou region, SW China. *Journal of Petroleum Science and Engineering, 165*, 199–211.

Li, F., Jiang, B., Song, Y., Cheng, G., & Lu, G. (2021). Multifractal behavior of the micro- and mesopore structures of brittle tectonically deformed coals and its influence on methane adsorption capacity. *Energy & Fuels, 35*, 3042–3064.

Liu, K., Ostadhassan, M., & Kong, L. (2018a). Multifractal characteristics of Longmaxi Shale pore structures by N 2 adsorption: A model comparison. *Journal of Petroleum Science and Engineering, 168*, 330–341.

Liu, K., Ostadhassan, M., Zou, J., Gentzis, T., Rezaee, R., Bubach, B., & Carvajal-Ortiz, H. (2018b). Multifractal analysis of gas adsorption isotherms for pore structure characterization of the Bakken Shale. *Fuel, 219*, 296–311.

Liu, X., & He, X. (2017). Effect of pore characteristics on coalbed methane adsorption in middle-high rank coals. *Adsorption, 23*, 3–12.

Liu, Y., Zhu, Y., Liu, S., Chen, S., Li, W., & Wang, Y. (2018c). Molecular structure controls on micropore evolution in coal vitrinite during coalification. *International Journal of Coal Geology, 199*, 19–30.

Mathews, J. P., & Sharma, A. (2012). The structural alignment of coal and the analogous case of Argonne Upper Freeport coal. *Fuel, 95*, 19–24.

Moore, T. A. (2012). Coalbed methane: A review. *International Journal of Coal Geology, 101*, 36–81.

Muller, J. (1996). Characterization of pore space in chalk by multifractal analysis. *Journal of Hydrology (amsterdam), 187*, 215–222.

Nie, B., Liu, X., Yang, L., Meng, J., & Li, X. (2015). Pore structure characterization of different rank coals using gas adsorption and scanning electron microscopy. *Fuel (guildford), 158*, 908–917.

Oluwadebi, A. G., Taylor, K. G., & Ma, L. (2019). A case study on 3D characterisation of pore structure in a tight sandstone gas reservoir: The Collyhurst Sandstone, East Irish Sea Basin, northern England. *Journal of Natural Gas Science and Engineering, 68*, 102917.

Pang, W., Wang, Y., & Jin, Z. (2021). Comprehensive review about methane adsorption in Shale Nanoporous media. *Energy & Fuels, 35*, 8456–8493.

Posadas, A. N. D., Giménez, D., Bittelli, M., Vaz, C. M. P., & Flury, M. (2001). Multifractal characterization of soil particle-size distributions. *Soil Science Society of America Journal, 65*, 1361–1367.

Rezaei, A., Siddiqui, F., Dindoruk, B., & Soliman, M. Y. (2020). A Review on Factors Influencing the Rock Mechanics of the Gas Bearing Formations. *Journal of Natural Gas Science and Engineering, 80*, 103348.

San Jos Martínez, F., Martín, M. A., Caniego, F. J., Tuller, M., Guber, A., Pachepsky, Y., & Garca-Gutiérrez, C. (2010). Multifractal analysis of discretized X-ray CT images for the characterization of soil macropore structures. *Geoderma., 156*, 32–42.

Sing, K. S. W. (1985). Reporting physisiorption data for gas/solid systems with special reference to the determination of Surface Area and Porosity. *Pure & Applied Chemistry, 57*, 603–619.

Sun, B., Yang, Q., Zhu, J., Shao, T., Yang, Y., Hou, C., & Li, G. (2020). Pore size distributions and pore multifractal characteristics of medium and low-rank coals. *Scientific Reports, 10*, 1–12.

Tao, S., Chen, S., Tang, D., Zhao, X., Xu, H., & Li, S. (2018). Material composition, pore structure and adsorption capacity of low-rank coals around the first coalification jump: A case of eastern Junggar Basin, China. *Fuel, 211*, 804–815.

Thommes, M., Kaneko, K., Neimark, A. V., Olivier, J. P., Rodriguez-Reinoso, F., Rouquerol, J., & Sing, K. S. W. (2015). Physisorption of gases, with special reference to the evaluation of surface area and pore size distribution (IUPAC Technical Report). *Pure and Applied Chemistry, 87*, 1051–1069.

Vázquez, E. V., Ferreiro, J. P., Miranda, J. G. V., & González, A. P. (2008). Multifractal analysis of pore size distributions as affected by simulated rainfall. *Vadose Zone Journal, 7*, 500–511.

Vishal, V., Chandra, D., Bahadur, J., Sen, D., Hazra, B., Mahanta, B., & Mani, D. (2019). Interpreting pore dimensions in gas shales using a combination of SEM imaging, small-angle neutron scattering, and low-pressure gas adsorption. *Energy & Fuels, 33*, 4835–5484.

Vranjes-Wessely, S., Misch, D., Issa, I., Kiener, D., Fink, R., Seemann, T., Liu, B., Rantitsch, G., & Sachsenhofer, R. F. (2020). Nanoscale pore structure of Carboniferous coals from the Ukrainian Donets Basin: A combined HRTEM and gas sorption study. *International Journal of Coal Geology, 224*, 103484.

Wang, F., Cheng, Y., Lu, S., Jin, K., & Zhao, W. (2014). Influence of coalification on the pore characteristics of middle-high rank coal. *Energy & Fuels, 28*, 5729–5736.

Yu, S., Bo, J., Pei, S., & Jiahao, W. (2018). Matrix compression and multifractal characterization for tectonically deformed coals by Hg porosimetry. *Fuel, 211*, 661–675.

Zhang, J., Wei, C., Yan, G., & Lu, G. (2019). Structural and fractal characterization of adsorption pores of middle–high rank coal reservoirs in western Yunnan and eastern Guizhou: An experimental study of coals from the Panguan syncline and Laochang anticline. *Energy Exploration & Exploitation, 37*, 251–272.

Zhang, M., Duan, C., Li, G., Fu, X., Zhong, Q., Liu, H., & Dong, Z. (2021). Determinations of the multifractal characteristics of the pore structures of low-, middle-, and high-rank coal using high-pressure mercury injection. *Journal of petroleum science & engineering, 203*, 108656.

Zhang, S., Wu, C., & Liu, H. (2020). Comprehensive characteristics of pore structure and factors influencing micropore development in the Laochang mining area, eastern Yunnan, China. *Journal of Petroleum Science and Engineering, 190*, 107090.

Zhang, Z., Qin, Y., Yi, T., You, Z., & Yang, Z. (2020b). Pore structure characteristics of coal and their geological controlling factors in Eastern Yunnan and Western Guizhou, China. *ACS Omega, 5*, 19565–19578.

Zhao, P., Wang, X., Cai, J., Luo, M., Zhang, J., Liu, Y., Rabiei, M., & Li, C. (2019). Multifractal analysis of pore structure of Middle Bakken formation using low temperature N2 adsorption and NMR measurements. *Journal of Petroleum Science and Engineering, 176*, 312–320.

Zhao, W., Wang, K., Wang, L., Cheng, Y., Dong, H., Li, B., & Dai, L. (2021). Influence of matrix size and pore damage path on the size dependence of gas adsorption capacity of coal. *Fuel, 283*, 119289.

Zhao, Y., Lin, B., Liu, T., Zheng, Y., Sun, Y., Zhang, G., & Li, Q. (2021). Multifractal analysis of coal pore structure based on NMR experiment: A new method for predicting T2 cutoff value. *Fuel, 283*, 119338.

Zhao, Y., Sun, Y., Liu, S., Chen, Z., & Yuan, L. (2018). Pore structure characterization of coal by synchrotron radiation nano-CT. *Fuel, 215*, 102–110.